Am J Cancer Res 2020;10(1):350-364
www.ajcr.us /ISSN:2156-6976/ajcr0104570

Original Article

Novel drug delivery system based on hollow mesoporous magnetic nanoparticles for head and neck cancers–targeted therapy *in vitro* and *in vivo*

Zhaoqiang Zhang[1*], Lin Zhuang[2*], Yi Lin[3*], Mengdie Yan[4], Jiahong Lv[5], Xiaolei Li[5], Han Lin[3], Ping Zhu[3], Qiuping Lin[5], Yue Xu[5]

[1]Department of Oral and Maxillofacial Surgery, Stomatological Hospital, Southern Medical University, Guangzhou, China; [2]State Key Laboratory of Optoelectronic Materials and Technologies, Guangdong Provincial Key Laboratory of Photovoltaics Technonogies, School of Physics and Engineering, Institute for Solar Energy Systems, Sun Yat-sen University, Guangzhou, China; [3]Department of Oral and Maxillofacial, Guanghua School of Stomatology, Hospital of Stomatology, Sun Yat-sen University, Guangzhou, China; [4]Department of Orthodontics, Haizhu Square Branch, Stomatological Hospital, Southern Medical University, Guangzhou, China; [5]Department of Orthodontics, Guanghua School of Stomatology, Hospital of Stomatology, Sun Yat-sen University, China. [*]Equal contributors.

Received November 6, 2019; Accepted December 16, 2019; Epub January 1, 2020; Published January 15, 2020

Abstract: Magnetic targeting delivery of anti-cancer drug with controlled drug release function has been recognized as a promising strategy for pursuit of the increased chemotherapeutic efficacy and reduced adverse effects. Superparamagnetic nano-carrier is proved to be an efficient manner for superficial tumor therapy like head and neck cancers. The anti-tumor effect of chemotherapy drug can be enhanced by combining with external magnet. Herein, we reported the fabrication and functionalization of biocompatible and superparamagnetic hollow mesoporous nanoparticles with magnetic targeting. The nanoparticles drug delivery system was constructed by surface-engineering polyacrylic acid (PAA) onto the superparamagnetic nanoparticles which can load bleomycin (BLM) both in the mesoporous structure and via bonding with PAA. The drug was targeted and retained to the focal area under the magnetic field with the nano-carriers, and released sustainably. Detailed investigations demonstrated that PAA-functionalized magnetite nanoparticles loading BLM could stimulate tumor cells to apoptosis locally. The drug loaded and delivery system endowed the anticancer drug with targeting capability *in vitro* and suppressed the growth of tumor *in vivo*. The present targeted drug delivery system is a rather simple method without sophisticated chemistry or materials engineering and is promising in contributing to the progress of nanotherapeutics toward efficient head and neck cancer treatment.

Keywords: Drug delivery system, nanoparticles, magnetic targeted, sustained releasing, head and neck cancers

Introduction

Squamous cell cancer of head and neck cancers (HNSCC) remains a significant public health problem and rank among the six leading cancers by incidence worldwide, with more than 630,000 new patients diagnosed annually resulting in more than 350,000 deaths every year [1]. Bleomycin (BLM) is one of the most effective antibiotic agents commonly used, alone or in combination with other chemotherapeutic regimens, in the treatment of HNSCC [2-4]. However, its administration has been hindered by its dose-limiting toxic side effects such as pulmonary fibrosis, impaired lung function, and Reynaud's phenomenon [5-7]. Among these, the considerable risk of pulmonary fibrosis frequently limits clinical application to maximize its antineoplastic effects, which might reduce the drug efficacy.

To reduce side effects and improve the therapeutic effect of BLM, many efforts have been directed towards the administration routes for BLM in order to improve the specific distribution to targeted tissues. Intratumoral chemotherapy with collagen gel formulation containing anti-tumoral drug has been used to treat accessible solid tumors of various types including HNSCC. Although the systemic toxicity of

intratumoral administration is minimal, its efficacy is highly dependent on the timing and frequency of the drug injections because of its rapid clearance from the tumor site, which depends on physicochemical properties of the drug loading system and biophysical events (interstitial pressure, extravasation, tissue access). Nanodelivery systems present great potential to overcome these known barriers and to improve the efficacy and safety of chemotherapy treatment [8-10]. For superficial tumor like HNSCC, magnetic drug targeting has proven to be a promising strategy are among the most promising materials being used as essential platforms for targeted drug delivery, imaging and monitoring of therapeutic efficacy. Superparamagnetic nanoparticles (MNPs), as one of the most promising nanoscale drug carriers, have been employed to accumulate drugs specifically to a diseased site under the control of an external magnetic field, minimizing the undesirable side effects [11-14]. However, the potential of nonporous and nonswellable MNPs as a drug carrier remains limited. Mesoporous nanoparticles, therefore, have attracted much attention for their unique properties, such as tunable nanoparticle size, uniform mesopores, porous interior amendable to drug loading, high surface area, and easily functionalizable surface, which make them highly suitable as a therapeutic delivery vehicle [15, 16]. Our previous studies have synthesized the MNPs with favorable qualities by a simple solvothermal method. The MNPs could be easily functionalized with carboxyl groups for optimal BLM drug loading [17]. However, the biological effect of the functionalized BLM-MNPs both *in vitro* and *in vivo* under the condition of cancer has not yet been reported in the open literature.

Herein, BLM A5 (one of the most effective divisions of BLM) was functionalized onto the mesoporous MNPs with PAA capsule, and the cytotoxicity of functionalized BLM-MNPs and their apoptosis assay on HNSCC were performed. Selective antitumor and targeted effects of BLM-MNPs were investigated *in vitro* and *in vivo* under the control of a constant magnetic field.

Methods and materials

Instruments and materials

$FeCl_3 \cdot 6H_2O$, CH3COONa, ethyleneglycol (EG), ETH, dimethylformamide (DMF), polyacrylic acid (PAA, MW: 3000), ethanol, isopropanol, 1-ethyl-3-(3-diethyl-aminopropyl) carbodiimide (EDAC), N-hydroxysuccinicacid, Dimethyl sulfoxide (DMSO) were purchased from Aladdin Chemical Reagent Co, Ltd (Shanghai, China) and BLM A5 hydrochloride were purchased from Harbin Bolai pharmaceutical company (Harbin, China). Water used throughout all experiments was purified with the Millipore system. All chemicals were of reagent grade and used without further purification. Trypsin-0.25% EDTA was obtained from Invitrogen, Inc. (CA, USA). Normal melting agarose and fetal bovine serum (FBS) were also purchased from Invitrogen, Inc. (CA, USA). The other chemical materials such as paraformaldehyde, dimethylbenzene, ethanol, Phosphate buffer saline (PBS), Triton X-100, methanol, ethidium bromide, tetrabromoethane (TBE), Tris-HCl, and Ethylene Diamine Tetraacetic (EDTA) were purchased from Merck (Kenilworth, USA). The cell Counting Kit (WST, Beijing Zoman Biotechnology Co., Ltd, China) was used to measure cell viability. The annexin V-FITC apoptosis detection kit and Apotosis DNA Ladder detection kit were obtained from KeyGen Biotech (Nanjing, China). DNA fragmentation assay for tumor cells was performed on a wide mini-sub GT cell (110 V, Biorad Co., USA) and observed by Gel Doc XR + (Biorad Co., USA). To perform histological examination of tumor tissues, related tissues removed from nude mice were frozen-sliced into thin sections (Leica CM1950, Germany) and observed by microscope (Zeiss, China).

Preparation of BLM-MNPs

BLM-MNPs were prepared as our previously reported method [17]. In brief, the spheric Fe_3O_4 nanoparticles with 30 nm in mean diameter were synthesized with the solvothermal approach. The $FeCl_3 \cdot 6H_2O$ dissolved in EG was mixed with NaAc and ETH under ultrasonic vibration before autoclave. After heating in autoclave, they are cooled to room temperature, purified and were added in distilled water to make a magnetic Fe_3O_4 nanoparticle sol with solid content of 20%. The sol was dispersed in DMF and mixed with PAA before another autoclave. Subsequently, isopropanol and ethanol was used to purify the product. The BLM was then loaded in 5% of the PAA-functionalized MNP under 2 h stirring at room temperature. The assembly of BLM-MNPs was shown in **Figure 1**.

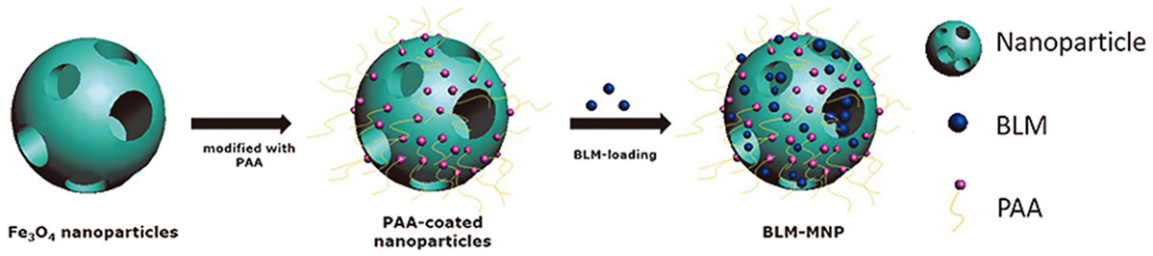

Figure 1. Schematic showing the synthesis of the nanoparticles drug delivery system of the magnetic nanoparticle with surface-engineering PAA in the outer layer and BLM molecules bonded with PAA.

Characterization of BLM-MNPs

Field emission scanning electron microscopy (FESEM, JSM-6330F; JEOL, Peabody, USA) was operated at an accelerating voltage of 20.00 kV. Transmission electron microscope (TEM, JEM-2010HR, 200 kV, JEOL Ltd) was operated to observe the morphology and sizes of the MNPs. TEM samples containing Fe_3O_4 were dispersed with n-hexane until it was about the color of 'weak tea'. A drop of it was added onto copper-coated grid and the n-hexane was evaporated. The magnetic properties (M-H curves) were measured at room temperature by the use of a Vibrating Sample Magnetometer (VSM, Lake Shore 7404, Cryotronics, Inc) at 300 K under an applied field of ±6000 g. The surface of the coated Fe_3O_4 was analyzed by XRD (Rigaku-Dmax 2500, Rigaku Corporation) with monochromatic Cu Kα radiation. Infrared (IR) spectra were recorded with wave numbers ranging from 4000 to 400 cm^{-1} with Fourier transformation infrared spectrometer (FT-IR, EQUINOX 55, Bruker Co.) coupled with infrared microscope with a resolution of 2 cm^{-1}.

BLM loading and release

The drug release behavior of the finally prepared drug-conjugated core-sphere nanoparticles was studied in physiological pH (7.4) as well as in acidic media with pH of 5.3. To make a control, the naked magnetic nanoparticles were also studied here in neutral and acidic media. Typically, 10 ml of BLM loaded magnetic nanoparticles coated with PAA with 2.5 mg of BLM were placed into a dialysis bag (MWCO: 8-14 kDa) and dialyzed against 150 mL of phosphate buffered saline (PBS) at 37°C under mild stirring (100 rpm). At predetermined time intervals, in order to determine the drug concentration, and thereby time dependent drug release profile, 5.0 mL of solution was taken out and replaced with 5.0 mL of fresh buffer solution maintained at 37°C and evaluated for drug content by UV-Vis spectroscopy at wavelength of 291 nm. The percent of drug release was calculated in reference to a control sample placed at the same condition, but without nanoparticles.

Cell culture

Human tongue carcinoma cells (Cal-27) were purchased from ATCC. Human nasopharyngeal carcinoma cells (CNE2) were purchased from Yansheng industrial co. Human Cal-27 tongue carcinoma cells were cultured in Dulbecco's Modified Eagle medium (DMEM) containing 10% fetal bovine serum and 1% antibiotics (100 units of penicillin and 100 mg streptomycin) in a humidified incubator at 37°C and in an atmosphere of 5% CO_2. CNE2 were cultured in RPMI-1640 medium. The cells were passaged every 2-3 days.

Magnetic targeted effect of BLM-MNPs

Since magnetic Fe_3O_4 nanoparticles exhibited high magnetic properties, we designed an *in vitro* experiment to examine the magnetic targeting effect of it. 4×10^4 Cal-27 cells were plated in a 60 mm culture dish and cultured under the same conditions as above for 24 h. A small round magnet, 5 mm in diameter, was placed at the center of the culture well with cells cultured with MNPs, BLM, and BLM-MNPs in complete medium. Cell growth status in magnetic and non-magnetic fields was observed under microscope at 24 h and 48 h. After incubation at 37°C for 24 h, the medium was aspirated and washed several times to remove the nanoparticles. Then the cells were collected after centrifugation and fixed in 4% glutaraldehyde for 2 h at 4°C. Subsequently, the cells were washed three times with sodium cacodyl-

ate buffer and post-fixed in 1% osmium tetroxide. Samples were dehydrated with gradient ethanol, and embedded in Epon. Thereafter, the samples were cut into ultrathin sections and were stained with uranyl acetate. The intake of BLM-MNPs within cells was observed by TEM.

Cell viability analysis

Cell Counting Kit-8 (CCK-8) assay was performed to evaluate whether the MNP were biocompatible and the effect of BLM-MNPs on tumor cells. 1.5×10^3/well Cal-27 or CNE2 cells were plated into 96-well culture plates. After sterilized by Ultraviolet radiation for 12 h, the MNPs, BLM, and BLM-MNPs were diluted with the cell culture medium to 10, 25, 50, 100 μg/mL, and then added into the cells and cultured to measure their growth and viability for another 12 h, 24 h, 48 h, and 72 h. After incubation, the medium was removed and 90 ul cell culture medium mixed with 10 ul CCK-8 solution were added to each well. After incubating in dark for 4 h at 37°C, the reading was done at 450 nm using enzyme-labeled instrument. The cell viability index in percentage was calculated as follows: the cell viability index (%) = (mean absorbency of experimental group at specific concentration - mean absorbency of negative control)/(mean absorbency of positive control - mean absorbency of negative control) expressed as a percentage.

Apoptosis analysis by DAPI staining, flow cytometry and DNA fragmentation in vitro

DAPI staining was carried out to detect a morphology change of the nuclei of Cal-27 cells. The cells were inoculated in a 24-well plate and then treated with MNPs, BLM, and BLM-MNPs for 24 h, respectively. The cells were then washed twice with PBS and fixed with 4% paraformaldehyde for 10 min. Thereafter, the cells were stained with DAPI for 15 min and observed under fluorescence microscope.

Cells were plated in a 6-well plate and cultured overnight at 37°C. After treatment of different drugs at 24 h, both the floating cells in the medium and attached cells were harvested by trypsinization. The cells were washed twice with PBS and incubated in 500 μl biding buffer containing 5 μl PI and 5 μl annexin for 10 min in darkness at room temperature. The apoptotic cells were detected by flow cytometer.

The cells were harvested and then lysed for 4 h at 60°C with a 500 μl lysis buffer (10 mM Tris-cl, 0.1M EDTA, 0.5% SDS) containing 20 mg/ml proteinase K and 10 mg/ml RNase A. Samples were vortexed for 10 s every hour. Subsequently, 500 μl Phenol, chloroform, and isoamyl alcohol at the ratio of 25:24:1 was added to each sample followed by centrifugation to get the DNA pellet. DNA was precipitated with 0.1 vol. 3 mol/L sodium acetate and 2.5 vol. cold ethanol. Finally, the DNA were air dried and dissolved in a TE buffer, separated by electrophoresis in 1.5% agarose gels containing ethidium bromide and visualized under ultraviolet light.

Establishment of tumor model on nude mice

Thirty-six female BALB-C nude mice were purchased from Laboratory Animals Centre of Sun Yat-sen University (Guangzhou, China). They were maintained in specific pathogen-free (SPF) facilities in the animal center. Animal experiments were carried out according to the Animal Management Rules of the Ministry of Health of the People's Republic of China (Document No. ERC-2014-1) and the guidelines for the Care and Use of Laboratory Animals of Sun Yat-sen University. Normal nude mice (average weight 19.3±0.3 g) were provided by Laboratory Animals Centre of Sun Yat-sen University (Guangzhou, China) for studies *in vivo*. Cal-27 cells (0.2 mL, 1.5×10^7 cells mL^{-1} in PBS) were injected in the subcutaneous tissue of the nude mice. Thereafter, all the treated nude mice were observed every day to monitor and measure the sizes of tumors, using a digital caliper. When the tumor size of the mice grew to an average volume of 25 mm^3, calculated by the formula volume = (tumor length) × (tumor width)^2/2, the mice with the tumor large enough were used for further studies. Among them, the mice with the maximum size and the minimum size of tumors were excluded.

Tumor assessment in vivo

In this study, 36 mice bearing square cell carcinoma were divided into four groups: normal saline (NS), MNPs, BLM, and BLM-MNPs. 50 μL of each of the above solution are injected intratumorally with targeted magnet fixed locally on the surface of the tumor. The mice treated with NS were acted as the blank control. Before injection, the tumor size and mouse weight were measured daily by a digital caliper and digital calculation balance. Tumor size was measured

three times a week using a vernier caliper in different groups. The tumor volume was calculated using the following equation: tumor volume (V) = length × width^2/2. Relative tumor volume was calculated as V/V_0 (V_0 was the initial tumour volume before any injection).

After treatment for 1 week and 3 weeks, three mice of each group were sacrificed and the tumor was removed from the nude mice for histological study. The tumor tissues were fixed in 10% neutral buffered formalin and embedded routinely into paraffin. Subsequently, they were sectioned at a thickness of 4 μm, stained with hematoxylin and eosin (H&E) and TdT-mediated dUTP Nick-End Labeling (TUNEL) according to the manufacturer's standardized protocols and examined by inverted phase contrast microscope and three random views in each section were selected for quantitative assay.

Results

Characterization of BLM-MNPs

SEM images of uncoated and PAA coated nanoparticles were spherical (**Figure 2A** and **2B**). TEM images indicated that the polyacrylic-acid-coated Fe_3O_4 nanoparticles displayed a thin polymeric shell, which is absent on uncoated nanoparticles. TEM measurements denoted that the diameters of the uncoated and polyacrylic-acid-coated nanoparticles were 30 and 45 nm, respectively. The particles are spherical in shape and well dispersed without aggregation, indicating good monodispersity of the particles (**Figure 2C** and **2D**). The magnetization curve, as shown in **Figure 2E**, was measured in powder samples of Fe_3O_4 nanoparticles at room temperature as the applied magnetic field (Oe) changed from -5000 Oe to 5000 Oe. Both the Fe_3O_4 nanoparticles and polymeric Fe_3O_4 nanoparticles exhibited negligible coercivity and remanence when the magnetic field was removed, implying magnetic nanoparticles were superparamagnetic. In the wide angle XRD spectrums (**Figure 2F**) of naked Fe_3O_4 nanoparticles (a) and BLM-MNPs (b), the diffraction peaks match well with the normal characteristic diffractions of the Fe_3O_4 inverse spinel structure (PCPDFWIN v.2.02, PDF No. 89-0691). The spectroscopy of naked Fe_3O_4 nanoparticles showed a characteristic absorption peak at 564 cm^{-1} related to Fe-O group. The peaks at 1712 cm^{-1}, 1542 cm^{-1}, and 1450 cm^{-1} in PAA in spectrum are related to COO- groups. The peak at 567 cm^{-1} in spectrum represents the Fe-O stretching vibration, and the peaks at 1712 cm^{-1}, 1587 cm^{-1}, and 1444 cm^{-1} prove the existence of PAA in the product particles (**Figure 2G**, Black: BLM; Blue: BLM-MNPs; Red: MNPs coated with PAA).

Drug releasing kinetics in vitro

Drug loading efficiency was 50.71±0.20%, which was comparable with our previous study [17]. The *in vitro* release profile of BLM from naked or functionalized Fe_3O_4 magnetic nanoparticles in acetate buffer solution (pH 5.0) and PBS (pH 7.2) were evaluated by dialysis method and are shown in **Figure 3**. Generally, all the groups released about 20% of the drug in the first 2 h except for the naked nanoparticles at pH 5.0 (10%). Nearly 50% of the loaded BLM was released after 24 h at pH 5.0, while at pH 7.2 the BLM release was up to approximately 70%. Most of the drugs (80%) were released before 48 h in all situations (**Figure 3**, *P<0.05).

Magnetic-targeting of BLM-MNPs on tumor cell in vitro

BLM-MNPs clustered around the magnet, manifesting as reduced cytotoxicity to normal cells at this area with the drug loaded on it (**Figure 4A**, **4B** showed the control group which was not under magnet). After 24 h, the number of cells declined considerably in magnetic field (**Figure 4D**, Black: BLM-MNPs), while cells outside the magnetic region continued to grow (**Figure 4C**). The amount of cells rebounded after 48 h (**Figure 4F**, Black: BLM-MNPs; **Figure 4E** showed the control group which was not under magnet) in the magnetic field probably due to the majority release before 48 h, which is in accordance with the results of the *in vitro* release profile.

TEM observation of BLM-MNPs on tumor cell in vitro

The mechanism for BLM-MNPs internalization within the Cal-27 cells was characterized by TEM. **Figure 5** showed the TEM images of cells after incubation of 24 hours with BLM-MNPs. The BLM-MNPs were observed mainly in the cytoplasm (**Figure 5A**, white arrow). More importantly, BLM-MNPs were found to be located inside the endosome (**Figure 5B**, white arrow). Interestingly, we detected that cells formed pseudopodia to endocytose nanoparticles. (**Figure 5C**, white arrow). After a long incu-

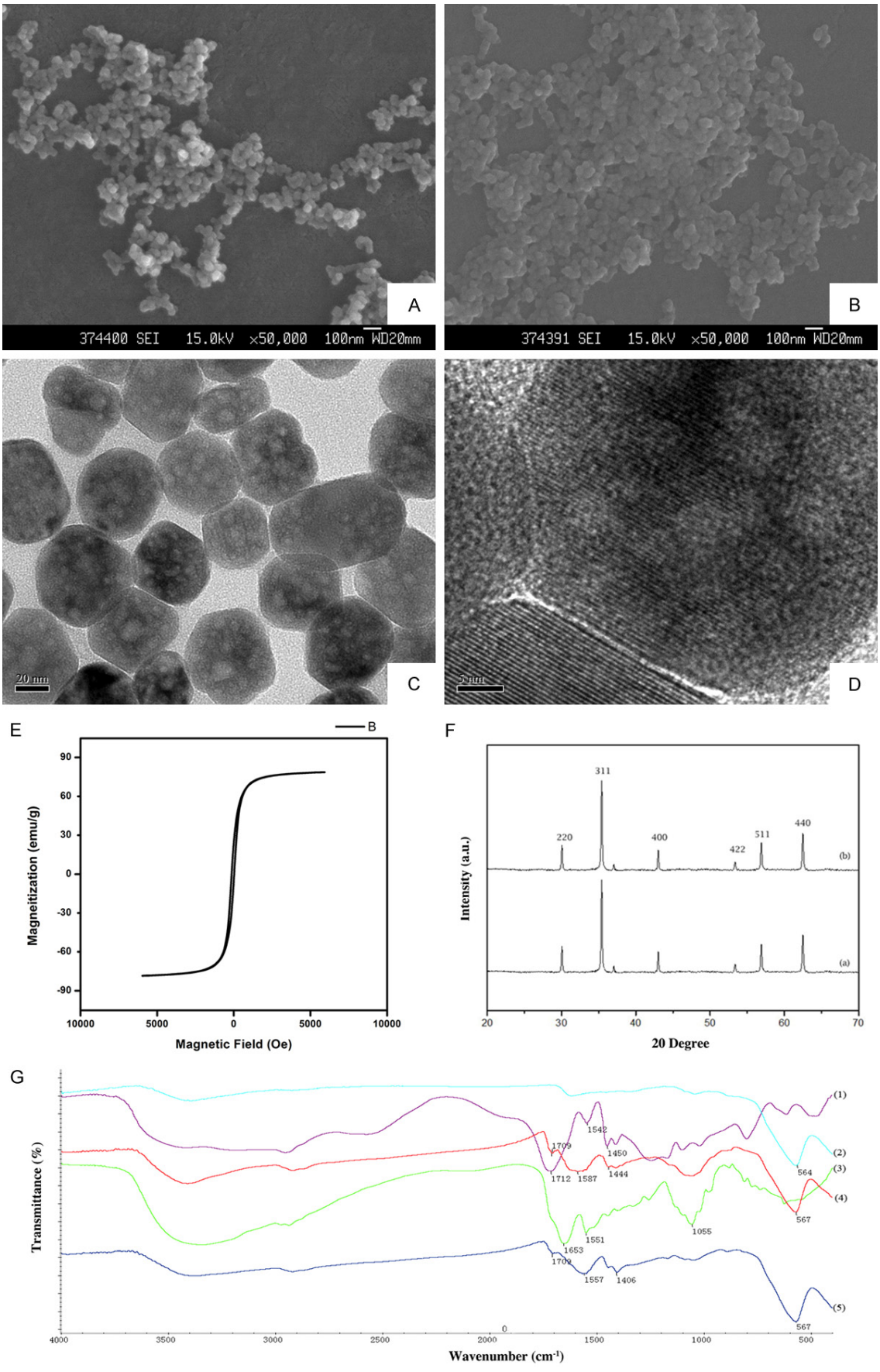
A
374400 SEI 15.0kV ×50,000 100nm WD20mm
B
374391 SEI 15.0kV ×50,000 100nm WD20mm
20 nm
C
5 nm
D
E
B
Magneitization (emu/g)
Magnetic Field (Oe)
F
311
220
400
422
511
440
(b)
(a)
Intensity (a.u.)
20 Degree
G
Transmittance (%)
Wavenumber (cm-1)
(1)
(2)
(3)
(4)
(5)
1709
1542
1450
1712
1587
1444
564
567
1055
1551
1653
1709
1557
1406
567

Figure 2. Characterizations of uncoated nanoparticles, functionalized MNPs and BLM-MNPs. (A) SEM image of uncoated nanoparticles. Bar = 100 nm. (B) SEM image of PAA-coated nanoparticles. Bar = 100 nm. (C) TEM image of uncoated nanoparticles. The nanoparticles were well-shaped sphere with multiple hollow mesoporous structures. Bar = 20 nm. (D) Amplified images of the regions of interest boxed in the corresponding left panels. Bar = 5 nm. The constant distance between the stripes on the magnetite particles was shown which could indicate specific crystallographic plane. (E) Magnetization curve of naked Fe_3O_4 nanoparticles. (F) XRD spectrums of naked Fe_3O_4 nanoparticles (A) and BLM-MNPs (B). (G) FT-IR spectrums of BLM, BLM-loaded nanoparticles, PAA-modified nanoparticles. The absorption peak around 564 cm^{-1} was related to Fe-O group; the peaks around 1542 cm^{-1} are related to COO- groups. (Black: BLM; Blue: BLM-MNPs; Red: MNPs coated with PAA).

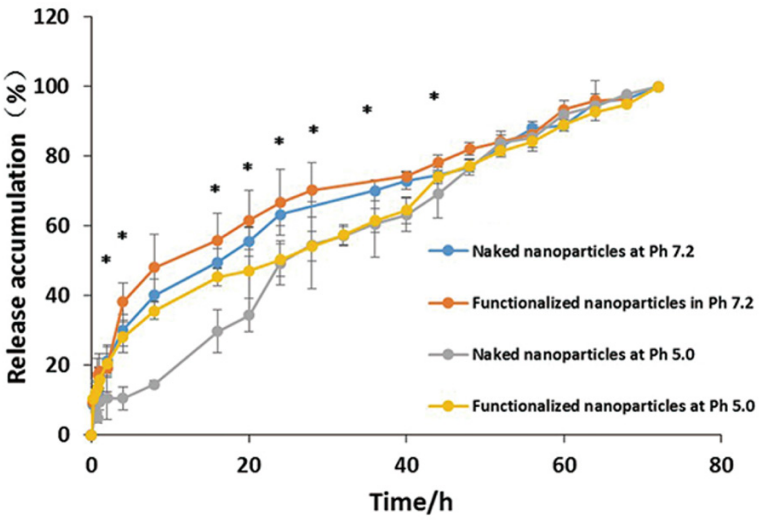

Figure 3. Drug release of naked nanoparticles versus PAA-coated nanoparticles at pH 7.2 & pH 5.0 respectively. Most of the drugs were released before 48 h in all situations. The systems in acidic condition display a slower drug release profile than in medium condition. And the functionalized nanoparticles system display faster release rate in 48 h (*P<0.05).

bation, a great number of BLM-MNPs were intruding into the nucleus of Cal-27 cells (**Figure 5D**, white arrow), and a great number of BLM-MNPs were situated inside the vesicles (**Figure 5E** and **5F**, white arrow). All these figures show that the cells successfully absorbed BLM-MNPs. The observation could be the explained by a fast diffusive internalization pathway, a mechanism only reported for small, charged nanoparticles.

Inhibitory effects of BLM-MNPs on tumor cell in vitro

In general, the cell viability decreased with incubation for MNPs, BLM, and BLM-MNPs by order on equal terms. **Figure 6A-D** (*P<0.05) shows that the cell viability of Cal-27 decreased subtly with the increased concentration of BLM and BLM-MNPs from 10 μg/mL to 100 μg/mL, while the decreasing tendencies are more prominent for BLM-MNPs that is followed by BLM. This phenomenon can be similarly seen in incremental incubation time (12 h, 24 h, 48 h and 72 h). **Figure 6E-G** (*P<0.05) shows that the cell viability of CNE2 decreased with the same tendency of Cal-27 from 10 μg/mL to 50 μg/mL. Our results found the cell viability nearly unchanged along with the time elapsed from 12 h to 72 h when incubating with MNPs, regardless of different concentrations. However, the cell viability declined dramatically with BLM-MNPs and BLM under the same concentration of particles.

Apoptosis analysis of BLM-MNPs on tumor cell in vitro

After 24 h of incubation of Cal-27 cells with NS (**Figure 7A**), MNPs (**Figure 7B**), BLM (**Figure 7C**) and BLM-MNPs (**Figure 7D**), the cells were fixed and processed using inverted fluorescence microscope. In the NS group, the nucleus was homogeneously stained and no DNA damage was observed. The nuclear blue fluorescence was also clear in the MNPs group (**Figure 7B**). After treatment with BLM and BLM-MNPs, the characteristics of apoptosis, such as nuclear fragmentation and chromatin condensation, were observed in the nucleus (**Figure 7C** and **7D**, white arrow).

Annexin V-FITC/PI dual staining was conducted to determine the proportion of apoptotic cells in each group. As shown in **Figure 7E** and **7F**, apoptotic rates in BLM-MNPs treated cells were significantly higher in contrast to BLM treated cells, and in BLM-MNPs treated cells were significantly higher in contrast to NS or MNPs treated cells (**Figure 7E** and **7F**,

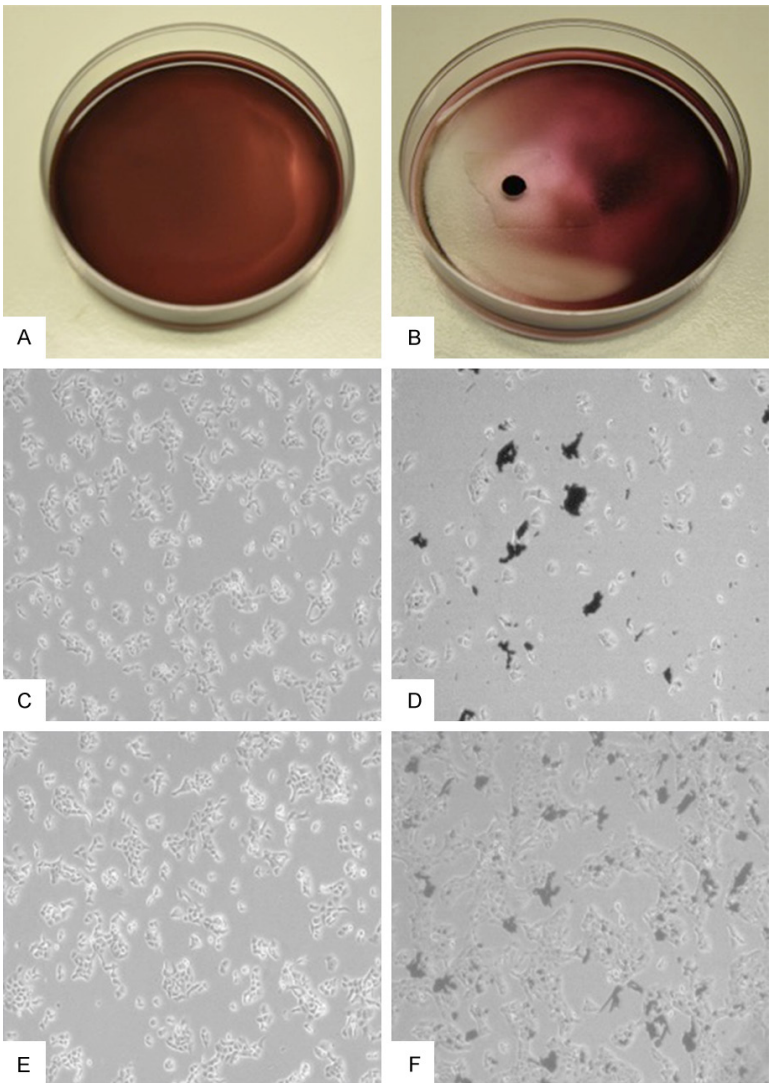

Figure 4. Magnetic-targeting effect of BLM-MNPs on tumor cell *in vitro*. A. Representative macroscopic image of Cal-27 cells treated with BLM-MNPs after 0 h of incubation; B. Representative macroscopic image of Cal-27 cells treated with BLM-MNPs after 0 h of incubation under magnet field. BLM-MNPs clustered around the magnet, manifesting as reduced cytotoxicity to normal cells at this area with the drug loaded on it; C. Representative microscopic image of Cal-27 cells treated with BLM-MNPs after 24 h; D. Representative microscopic image of Cal-27 cells treated with BLM-MNPs after 24 h of incubation under magnet field, the number of cells declined considerably in magnetic field (Black: BLM-MNPs); E. Representative microscopic image of Cal-27 cells treated with BLM-MNPs after 48 h of incubation; F. Representative microscopic image of Cal-27 cells treated with BLM-MNPs after 48 h of incubation under magnet field (Black: BLM-MNPs).

*P<0.05). These results have clearly demonstrated that BLM-MNPs has the apoptosis effect on Cal-27 and CNE2 cells.

The DNA fragmentation in Cal-27 cells with or without the treatment of drugs was detected by agarose gel electrophoresis. After incubation for 24 h, characteristics of apoptosis (DNA ladder bands) were detectable in BLM-MNPs and BLM groups. No DNA fragmentation was detected when cells were exposed to MNPs or NS (**Figure 7G**).

Inhibitory effect of BLM-MNPs on tumors under the control of magnetic field in vivo

To finally investigate the inhibitory effect of BLM-MNPs on tumors *in vivo*, tumor models on nude mice were established by injection of Cal-27 cells into subcutaneous tissues. After injection for 1 week, nude mice (around 19-20 g) with similar tumor size were utilized to carry out the studies. We periodically measured the mice's weights after tail injections of NS, BLM, MNPs and BLM-MNPs. The mice treated with NS were used as the control group. Every group had six duplicate mice samples (n = 6). In the initial stage, the weights of nude mice were recorded to be approximately 19.4±0.9 g. All the injections were administered three times per week. As shown in **Figure 8B** (*P<0.05), the mice still maintained their weight around 20 g after an injection of MNPs, similar to the group injected with BLM, while the latter even continued to grow and feed for 21 days. However, the average weights of the mice treated with NS and BLM-MNPs increased to 22.1 g and 22.2 g, respectively. The results indicate that MNPs had a good biocompatibility and could reduce the side effects of BLM on nude mice when they were targeted by a magnetic field. We then measured the tumor sizes at fixed time intervals in order to investigate tumor growth after

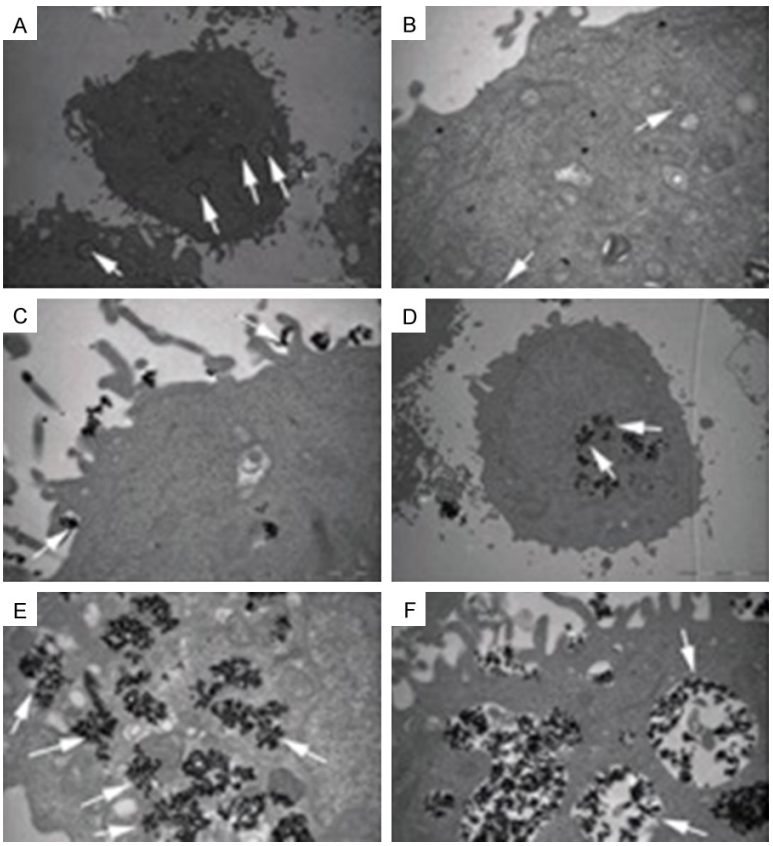

Figure 5. TEM images of Cal-27 treated with BLM-MNPs after 24 h of incubation. A. The BLM-MNPs were observed mainly in the cytoplasm (white arrows indicate diffusive nanoparticles, scale bar: 5 μm); B. The BLM-MNPs were found to be located inside the endosome (white arrow, scale bar: 5 μm); C. Cal-27 cells formed pseudopodia to endocytose BLM-MNPs (white arrow, scale bar: 1 μm); D. A great number of BLM-MNPs were intruding into the nucleus of Cal-27 cells (white arrow, scale bar: 1 μm); E, F. A great number of BLM-MNPs were situated inside the vesicles (white arrow, scale bar: 1 μm).

injection with BLM and BLM-MNPs, with or without magnetic targeting. Quantitative analysis showed that *in vivo* tumor sizes increased upon feeding time after treatment with NS and MNPs, BLM, and BLM-MNPs, respectively. As compared with the control groups of NS and other groups, the growth of tumor sizes was inhibited when treated with BLM and BLM-MNPs (**Figure 8A**). Inhibitory effect of BLM-MNPs with magnetic targeting on the surface of the nude mice tumors was better than without magnetic targeting, or of pure BLM. BLM-MNPs with magnetic targeting could efficiently inhibit the growth of tumors after curing for 14 days (**Figure 8C**, red circle showed the tumors). HE staining of the tumor sections indicate distribution of MNPs, showing that the group injected with BLM-MNPs with target had more particles remained and less cell population than others (**Figure 8D**). Tunnel assay further confirmed the antitumor potency of BLM-MNPs with target (**Figure 8E**, Blue: normal nucleus; brown: apoptosis positive cell nucleus). Tumors of mice treated with BLM-MNPs with target showed apoptosis at high proportion compared with other groups, even for the group treated with BLM (**Figure 8F**, *P<0.05).

Discussion

Our previous studies have demonstrated that BLM-MNPs combined drug system functionalized by PAA in a medium solution has favorable adsorption and releasing ability [17]. However, the biological effect of the functionalized BLM-MNPs on head and neck cancers is not clear. Herein, the cytotoxicity of functionalized BLM-MNPs and their apoptosis assay on tongue square cell carcinoma (TSCC) were performed.

Spherical magnetite nanoparticles can offer a uniform surface area for the coating and conjugation of targeting ligands or therapeutic agents [18]. Particles ranging from 10 to 100 nm are optimal for systemic administration and demonstrate the most prolonged blood circulation times. Moreover, these nanoparticles have mesoporous structures on their surfaces with the porous size of 5-10 nm [19]. Mesoporous pores on the surfaces of Fe_3O_4 nanoparticles play an important role in increasing drug loading amounts and making nanoparticles effective magnetic carriers for drug targeting [20]. Therefore, the nanoparticles we have synthesized are promising candidates for successful drug loading and delivery. Superparamagnetism is an especially important property essential for magnetic targeting carriers, due to the prevention of capillary blockage by aggregations formed from residue magnetism after the applied field [21, 22]. Previous studies showed that a static magnetic

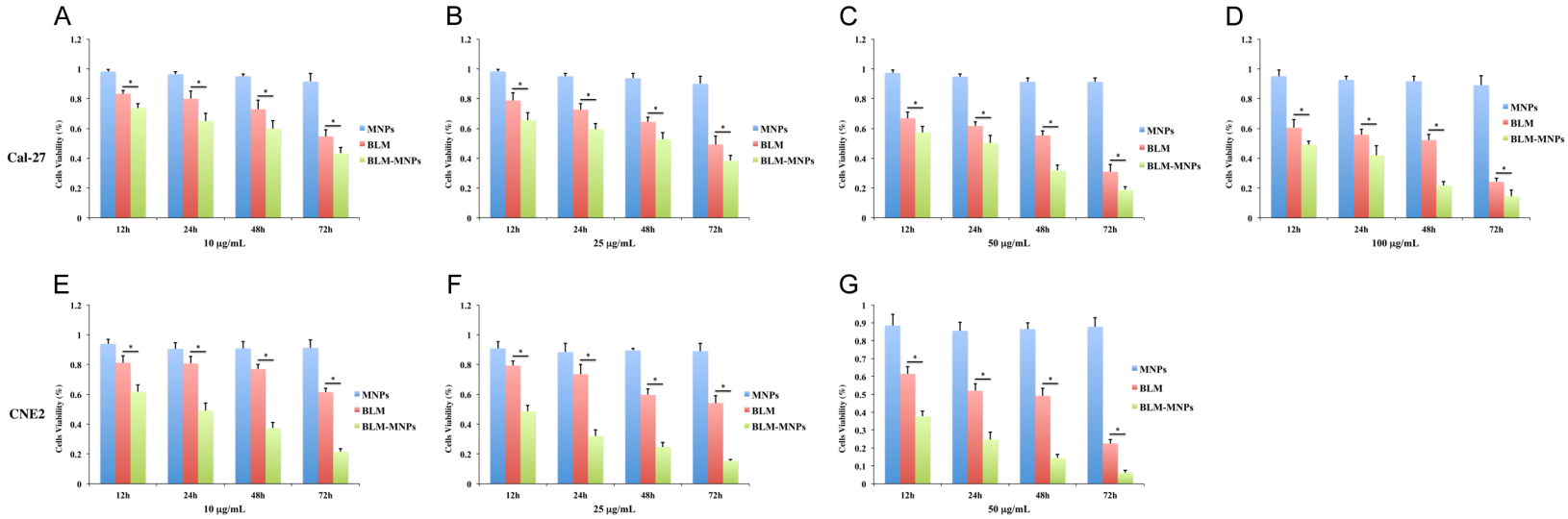

Figure 6. Inhibitory effects of BLM-MNPs on tumor cell *in vitro*. (A-G) Percentage of living cells after 12 h, 24 h, 48 h, 72 h of incubation with MNPs (blue bars), BLM (red bars), BLM-MNPs (green bars). The cell viability of Cal-27 (A-D) decreased subtly with the increased concentration of BLM and BLM-MNPs from 10 μg/mL to 100 μg/mL, while the decreasing tendencies are more prominent for BLM-MNPs that is followed by BLM. This phenomenon can be similarly seen in incremental incubation time (12 h, 24 h, 48 h and 72 h). The cell viability of CNE2 (E-G) decreased with the same tendency of Cal-27 from 10 μg/mL to 50 μg/mL (*P<0.05).

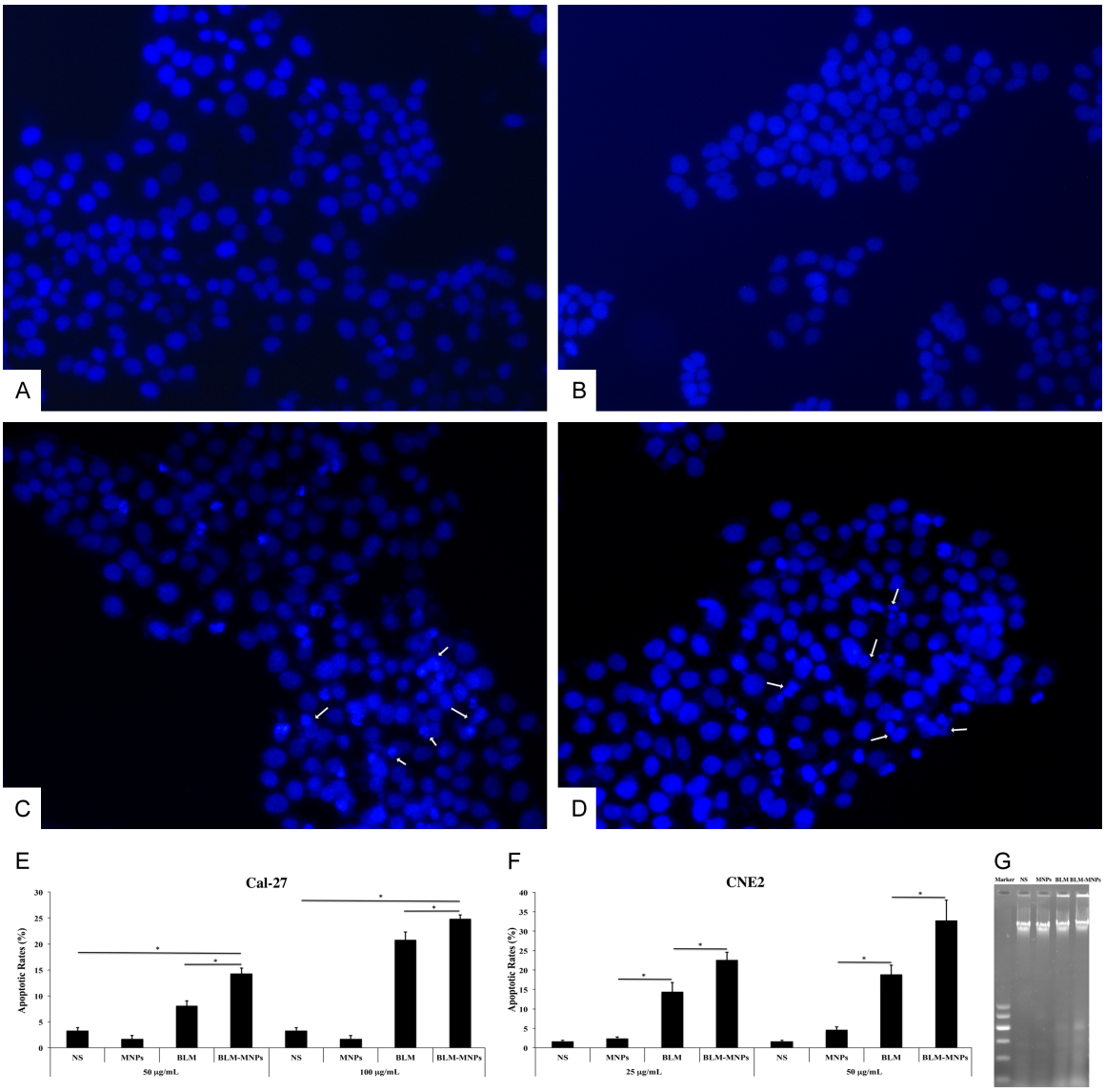

Figure 7. Apoptosis assay of BLM-MNPs on tumor cell *in vitro*. (A-D) Localization of nucleus, which was stained with 4',6-diamidino-2-phenylindole (DAPI). In the NS group (A), the nucleus was homogeneously stained and no DNA damage was observed. The nuclear blue fluorescence was also clear in the MNPs group (B). After treatment with BLM (C) and BLM-MNPs (D), the characteristics of apoptosis, such as nuclear fragmentation and chromatin condensation, were observed in the nucleus (C and D, white arrow); (E, F) The effect of BLM-MNPs on apoptotic rate of Cal-27 and CNE2 cells were detected by flow cytometry in comparison with NS, MNPs and BLM. 24 h of treatment with MNPs resulted in few apoptotic cells. The apoptotic rates in BLM-MNPs treated cells were significantly higher in contrast to BLM treated cells, and in BLM-MNPs treated cells were significantly higher in contrast to NS or MNPs treated cells (*P<0.05). These results have clearly demonstrated that BLM-MNPs has the apoptosis effect on Cal-27 and CNE2 cells. (G) After incubation for 24 h, characteristics of apoptosis (DNA ladder bands) were detectable in BLM-MNPs and BLM groups. No DNA fragmentation was detected when cells were exposed to MNPs or NS.

field as strong as up to 10 tesla did not show a negative impact on cell growth and cell cycles [23-25]. However, the *in vivo* safety of a magnetic field of >10 tesla has yet to be demonstrated [26]. External magnetic fields can enhance the accumulation of magnetic particles in tumors by the EPR effect. The materials synthesized in this study can be ideal candidates for developing delivery systems because of their excellent biocompatibility and superparamagnetism that enables long-term accumulation/retention at target sites by utilization of a suitable magnet, which is extremely important for practical applications in the biological and

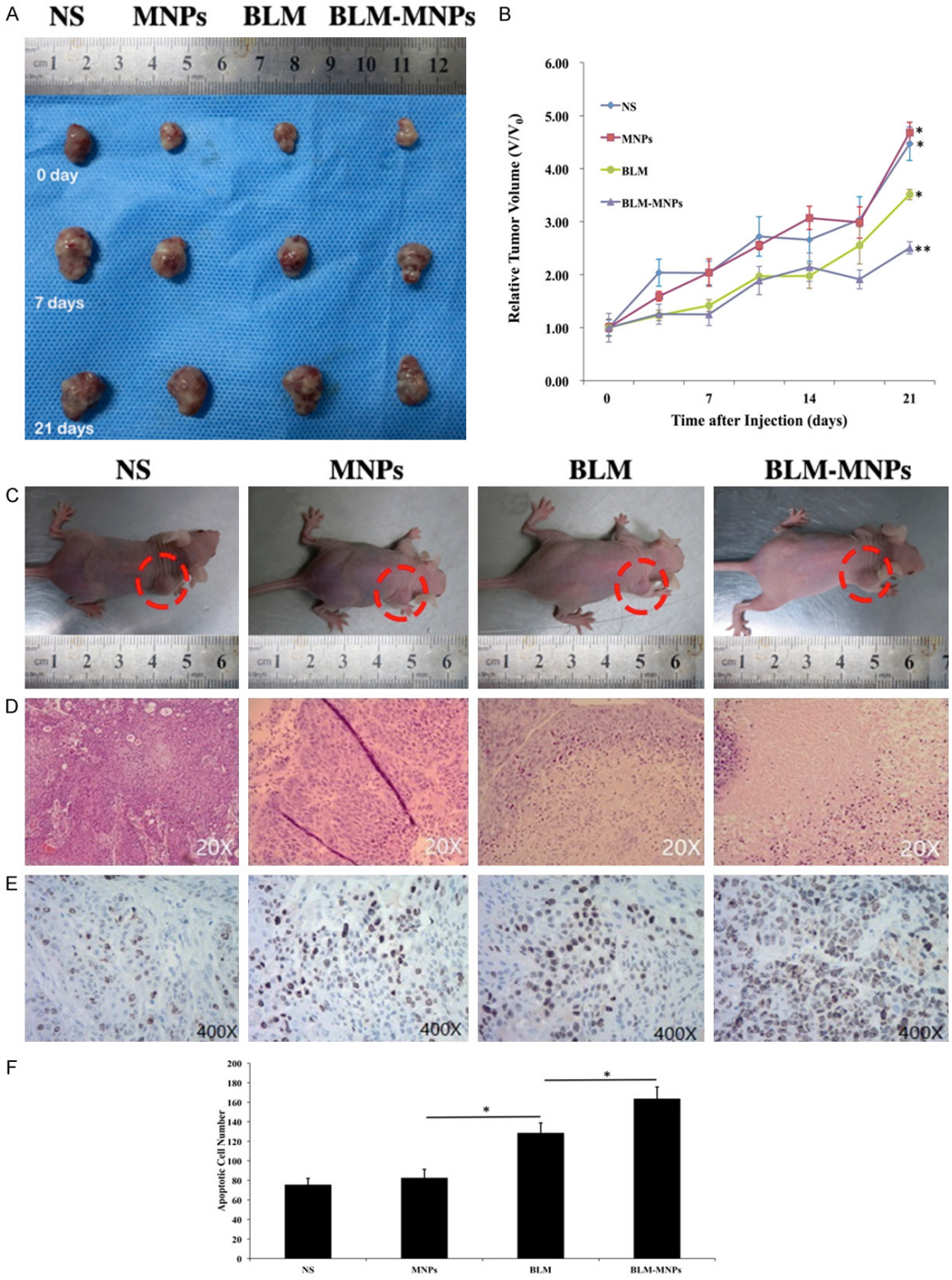

Figure 8. Inhibitory effect of BLM-MNPs on tumors under the control of magnetic field *in vivo*. A. Representative photographs of tumor from different groups at the beginning, 7th, 21th day, respectively; B. Relative tumor volume of different groups of mice after various treatments indicated (6 mice per group): mice injected with NS, MNPs, BLM and BLM-MNPs (*P<0.05); C. Representative photographs of the nude mice from different groups after curing for 14 days (red circle showed the tumors); D. H&E-stained tumor slices collected from different groups of mice on the following day after various treatments; E. Tunnel assay further confirmed the antitumor potency of BLM-MNPs with target (Blue: normal nucleus; brown: apoptosis positive cell nucleus). F. Tumors of mice treated with BLM-MNPs with target showed apoptosis at high proportion compared with other groups, even for the group treated with BLM (*P<0.05).

biomedical fields [27]. In addition, this system in acidic conditions displayed a slower drug release profile that is a desirable attribute for response to specific tumoral extracellular signatures [28]. Additionally, the faster release rate of functionalized nanoparticles is beneficial to intracellular release of anticancer drugs due to the acidic environment in endosomes and lysosomes (5.0-5.5) [29-31].

Our results found the cell viability nearly unchanged along with the time elapsed from 12 h to 72 h when incubating with MNPs, regardless of different concentrations. Yet cell viability declined dramatically with BLM-MNPs. The results indicate that the strong decrease in the number of living cells with BLM-MNPs can be mainly explained by a growth arrest, caused by interactions between concentrated and sustained-release BLM from BLM-MNPs and the nucleus. By contrast, MNPs showed almost no cytotoxic affect for the same nanoparticle concentrations, which in turns proved its biocompatibility.

From the results shown in **Figure 4**, BLM-MNP gathered in the targeted area, which explained that magnetic nanoparticles could deliver antitumor drugs to the targeted area in a magnetic environment and reduce cytotoxicity to normal cells. After 24 h, the number of cells was greatly reduced in the magnetic field, while cells in the non-magnetic field region continued to grow. The black material was magnetic nanoparticles.

All results shown in **Figure 8** indicate that pure BLM could not easily reach tumor sites and interact with tumor cells *in vivo*. After injection, BLM could only retain a transient high plasma drug concentration for a short time. BLM caused some damage or severe side effects to the normal cells and tissues *in vivo*. Then, free BLM was quickly distributed into other tissue organs, lost its bioactivity, and was finally excreted out of body via blood circulation and metabolism. To some extent, BLM-MNPs with local magnetic targeting was retained at a certain level through sustained release when the mice were injected. Although BLM-MNPs might relieve some side effects of BLM on the body, BLM still cannot be sustained for a long time at the target tumor tissues without magnetic attraction when combined with MNPs. Interestingly, BLM-MNPs with magnetic targeting efficiently inhibited the growth of tumor tissues on nude mice, especially after the second week. The mechanism could be interpreted as the magnetic field being able to gather BLM-MNPs constantly in the tumor tissue, allowing it to release BLM locally and steadily [32, 33]. BLM-MNPs with target group exhibited higher BLM-induced chemotoxicity than those without targeting BLM to the specific site. We conclude that this higher chemotoxicity is due to the efficient release of BLM and magnetic concentration triggered by mesoporous MNPs *in vivo*. This system takes advantage of the ability of the PAA polymer shell to reduce the inherent clearance of MNPs, and incorporation of a protease-cleavable moiety achieves constant delivery that stable tumor-localized drug release [34].

Immunohistochemistry of resected tumors further confirmed the antitumor potency of BLM-MNPs with target. Tumors of mice treated with BLM-MNPs with target showed apoptosis at high proportion, while mice receiving other treatments had tumors with large amount of viable cancer cells, even for the group treated with BLM. The results denote that conventional BLM administration isn't of capability to gather around the lesion location. In contrast, BLM-MNPs display a trend toward tumor site in which the external magnetic field was implemented and then release antineoplastic drug exerting powerful inhibitory effect on tumor cells. Nuclear fragmentation was also prominently displayed; suggesting BLM-MNPs access to nuclei and release BLM to damage DNA structure initiating apoptosis procedure.

In conclusion, the drug loaded and delivery system endowed the anticancer drug with targeting capability *in vitro* and inhibited the tumor growth with minimal side effects *in vivo*. The present targeted drug delivery system is a rather simple method without sophisticated chemistry or materials engineering and is promising in paving the way for the development of nanotherapeutics toward efficient cancer treatment.

Acknowledgements

This work was supported by the National Natural Science Foundation of China (81571020 and 81771124); Natural Science Foundation of Guangdong Province, China (No. 2018A03-0313759); Science Foundation of SMU (PY-

2017N036); Medical Scientific Research Foundation of Guangdong Province, China (A2018-358).

Disclosure of conflict of interest

None.

Address correspondence to: Dr. Yue Xu, Department of Orthodontics, Guanghua School of Stomatology, Sun Yat-sen University, No. 56 Lingyuan Xilu, Guangzhou 510055, China. Tel: +86-13660661-857; Fax: +86-020-83870387; E-mail: kou9315@hotmail.com

References

[1] Vigneswaran N and Williams MD. Epidemiologic trends in head and neck cancer and aids in diagnosis. Oral Maxillofac Surg Clin North Am 2014; 26: 123-141.

[2] Pendleton KP and Grandis JR. Cisplatin-based chemotherapy options for recurrent and/or metastatic squamous cell cancer of the head and neck. Clin Med Insights Ther 2013; 2013.

[3] Minicucci EM, da Silva GN and Salvadori DM. Relationship between head and neck cancer therapy and some genetic endpoints. World J Clin Oncol 2014; 5: 93-102.

[4] Pfister DG, Spencer S, Brizel DM, Burtness B, Busse PM, Caudell JJ, Cmelak AJ, Colevas AD, Dunphy F, Eisele DW, Gilbert J, Gillison ML, Haddad RI, Haughey BH, Hicks WL Jr, Hitchcock YJ, Jimeno A, Kies MS, Lydiatt WM, Maghami E, Martins R, McCaffrey T, Mell LK, Mittal BB, Pinto HA, Ridge JA, Rodriguez CP, Samant S, Schuller DE, Shah JP, Weber RS, Wolf GT, Worden F, Yom SS, McMillian NR and Hughes M; National Comprehensive Cancer Network. Head and neck cancers, Version 2.2014. Clinical practice guidelines in oncology. J Natl Compr Canc Netw 2014; 12: 1454-87.

[5] Shippee BM, Bates JS and Richards KL. The role of screening and monitoring for bleomycin pulmonary toxicity. J Oncol Pharm Pract 2016; 22: 308-312.

[6] Della Latta V, Cecchettini A, Del Ry S and Morales MA. Bleomycin in the setting of lung fibrosis induction: from biological mechanisms to counteractions. Pharmacol Res 2015; 97: 122-30.

[7] Azambuja E, Fleck JF, Batista RG and Menna Barreto SS. Bleomycin lung toxicity: who are the patients with increased risk? Pulm Pharmacol Ther 2005; 18: 363-6.

[8] Sanna V, Pala N and Sechi M. Targeted therapy using nanotechnology: focus on cancer. Int J Nanomedicine 2014; 9: 467-83.

[9] Frank D, Tyagi C, Tomar L, Choonara YE, du Toit LC, Kumar P, Penny C and Pillay V. Overview of the role of nanotechnological innovations in the detection and treatment of solid tumors. Int J Nanomedicine 2014; 9: 589-613.

[10] Jain S, Doshi AS, Iyer AK and Amiji MM. Multifunctional nanoparticles for targeting cancer and inflammatory diseases. J Drug Target 2013; 21: 888-903.

[11] Siafaka PI, Üstündağ Okur N, Karavas E and Bikiaris DN. Surface modified multifunctional and stimuli responsive nanoparticles for drug targeting: current status and uses. Int J Mol Sci 2016; 17.

[12] Laurent S, Saei AA, Behzadi S, Panahifar A and Mahmoudi M. Superparamagnetic iron oxide nanoparticles for delivery of therapeutic agents: opportunities and challenges. Expert Opin Drug Deliv 2014; 11: 1449-70.

[13] Singh A and Sahoo SK. Magnetic nanoparticles: a novel platform for cancer theranostics. Drug Discov Today 2014; 19: 474-81.

[14] Wang Y and Gu H. Core-shell-type magnetic mesoporous silica nanocomposites for bioimaging and therapeutic agent delivery. Adv Mater 2015; 27: 576-85.

[15] Angelos S, Khashab NM, Yang YW, Trabolsi A, Khatib HA, Stoddart JF and Zink JI. pH clock-operated mechanized nanoparticles. J Am Chem Soc 2009; 131: 12912-4.

[16] Zhao YL, Li Z, Kabehie S, Botros YY, Stoddart JF and Zink JI. pH-operated nanopistons on the surfaces of mesoporous silica nanoparticles. J Am Chem Soc 2010; 132: 13016-25.

[17] Xu Y, Lin Y, Zhuang L, Lin J, Lv J, Huang Q and Sun J. Bleomycin loaded magnetite nanoparticles functionalized by polyacrylic acid as a new antitumoral drug delivery system. Biomed Res Int 2013; 2013: 462589.

[18] Thomas CR, Ferris DP, Lee JH, Choi E, Cho MH, Kim ES, Stoddart JF, Shin JS, Cheon J and Zink JI. Noninvasive remote-controlled release of drug molecules in vitro using magnetic actuation of mechanized nanoparticles. J Am Chem Soc 2010; 132: 10623-10625.

[19] Du L, Liao S, Khatib HA, Stoddart JF and Zink JI. Controlled-access hollow mechanized silica nanocontainers. J Am Chem Soc 2009; 131: 15136-15142.

[20] Liu J, Bu W, Pan L and Shi J. NIR-triggered anticancer drug delivery by upconverting nanoparticles with integrated azobenzene-modified mesoporous silica. Angew Chem Int Engl 2013; 52: 4375-4379.

[21] Huang X and Du X. Pillar[6]arene-valved mesoporous silica nanovehicles for multiresponsive controlled release. ACS Appl Mater Interfaces 2014; 6: 20430-6.

[22] Hwang AA, Lu J, Tamanoi F and Zink JI. Functional nanovalves on protein-coated nanopar-

ticles for in vitro and in vivo controlled drug delivery. Small 2015; 11: 319-28.
[23] Ambrogio MW, Thomas CR, Zhao YL, Zink JI and Stoddart JF. Mechanized silica nanoparticles: a new frontier in theranostic nanomedicine. Acc Chem Res 2011; 44: 903-13.
[24] Lee HJ, Lee SJ, Uthaman S, Thomas RG, Hyun H, Jeong YY, Cho CS and Park IK. Biomedical applications of magnetically functionalized organic/inorganic hybrid nanofibers. Int J Mol Sci 2015; 16: 13661-77.
[25] Cheng YJ, Luo GF, Zhu JY, Xu XD, Zeng X, Cheng DB, Li YM, Wu Y, Zhang XZ, Zhuo RX and He F. Enzyme-induced and tumor-targeted drug delivery system based on multifunctional mesoporous silica nanoparticles. ACS Appl Mater Interfaces 2015; 7: 9078-87.
[26] Li QL, Sun Y, Sun YL, Wen J, Zhou Y, Bing QM, Isaacs LD, Jin Y, Gao H and Yang YW. Mesoporous silica nanoparticles coated by layer-by-layer self-assembly using cucurbit[7]uril for in vitro and in vivo anticancer drug release. Chem Mater 2014; 26: 6418-6431.
[27] Luo Z, Ding X, Hu Y, Wu S, Xiang Y, Zeng Y, Zhang B, Yan H, Zhang H, Zhu L, Liu J, Li J, Cai K and Zhao Y. Engineering a hollow nanocontainer platform with multifunctional molecular machines for tumor-targeted therapy in vitro and in vivo. ACS Nano 2013; 7: 10271-84.
[28] Yoshioka T, Chávez-Valdez A, Roether JA, Schubert DW and Boccaccini AR. AC electrophoretic deposition of organic-inorganic composite coatings. J Colloid Interface Sci 2013; 392: 167-71.
[29] Fazeli Sangani M, Owens G and Fotovat A. Transport of engineered nanoparticles in soils and aquifers. Environmental Reviews 2018; 27: 43-70.
[30] Bodratti AM and Alexandridis P. Amphiphilic block copolymers in drug delivery: advances in formulation structure and performance. Expert Opin Drug Deliv 2018; 15: 1085-1104.
[31] Bodratti AM and Alexandridis P. Formulation of poloxamers for drug delivery. J Funct Biomater 2018; 9.
[32] Lojk J, Bregar VB, Rajh M, Miš K, Kreft ME, Pirkmajer S, Veranič P and Pavlin M. Cell type-specific response to high intracellular loading of polyacrylic acid-coated magnetic nanoparticles. Int J Nanomedicine 2015; 10: 1449-62.
[33] Couto D, Sousa R, Andrade L, Leander M, Lopez-Quintela MA, Rivas J, Freitas P, Lima M, Porto G, Porto B, Carvalho F and Fernandes E. Polyacrylic acid coated and non-coated iron oxide nanoparticles are not genotoxic to human T lymphocytes. Toxicol Lett 2015; 234: 67-73.
[34] Booth A, Størseth T, Altin D, Fornara A, Ahniyaz A, Jungnickel H, Laux P, Luch A and Sørensen L. Freshwater dispersion stability of PAA-stabilised cerium oxide nanoparticles and toxicity towards Pseudokirchneriella subcapitata. Sci Total Environ 2015; 505: 596-605.